



# HHS Public Access

Author manuscript

*J Mol Cell Cardiol.* Author manuscript; available in PMC 2016 July 01.

Published in final edited form as:

*J Mol Cell Cardiol.* 2015 July ; 84: 170–178. doi:10.1016/j.yjmcc.2015.04.022.

## t-tubule disease: Relationship between t-tubule organization and regional contractile performance in human dilated cardiomyopathy

David J. Crossman, PhD<sup>1</sup>, Alistair A. Young, PhD<sup>2</sup>, Peter N. Ruygrok, MD<sup>3</sup>, Guy P. Nason, PhD<sup>4</sup>, David Baddeley, PhD<sup>1,5</sup>, Christian Soeller, PhD<sup>1,6</sup>, and Mark B. Cannell, PhD<sup>1,7,\*</sup>

<sup>1</sup>Department of Physiology, University of Auckland NZ

<sup>2</sup>Department of Anatomy with Radiology, University of Auckland NZ

<sup>3</sup>Department of Cardiology, Auckland City Hospital NZ

<sup>4</sup>School of Mathematics, University of Bristol, UK

<sup>7</sup>School of Physiology and Pharmacology, University of Bristol, UK

### Abstract

Evidence from animal models suggest that t-tubule changes may play an important role in the contractile deficit associated with heart failure. However samples are usually taken at random with no regard as to regional variability present in failing hearts which leads to uncertainty in the relationship between contractile performance and possible t-tubule derangement. Regional contraction in human hearts was measured by tagged cine MRI and model fitting. At transplant, failing hearts were biopsy sampled in identified regions and immunocytochemistry was used to label t-tubules and sarcomeric z-lines. Computer image analysis was used to assess 5 different unbiased measures of t-tubule structure/organization. In regions of failing hearts that showed good contractile performance, t-tubule organization was similar to that seen in normal hearts, with worsening structure correlating with the loss of regional contractile performance. Statistical analysis showed that t-tubule direction was most highly correlated with local contractile performance, followed by the amplitude of the sarcomeric peak in the Fourier transform of the t-tubule image. Other area based measures were less well correlated. We conclude that regional contractile performance in failing human hearts is strongly correlated with the local t-tubule organization. Cluster tree analysis with a functional definition of failing contraction strength allowed a pathological definition of 't-tubule disease'. The regional variability in contractile

© 2015 Published by Elsevier Ltd.

\*Address all correspondence to Mark B. Cannell, Professor of Cardiac Cell Biology, School of Physiology & Pharmacology, Medical Sciences Building, University of Bristol, Bristol, BS8 1TD, UK. mark.cannell@bristol.ac.uk.

<sup>5</sup>Department of Cell Biology, Yale University, New Haven, CT 06520-8002 USA

<sup>6</sup>Biomedical Physics, University of Exeter, Exeter EX4 4SB, UK

### Disclosure statement

None declared.

**Publisher's Disclaimer:** This is a PDF file of an unedited manuscript that has been accepted for publication. As a service to our customers we are providing this early version of the manuscript. The manuscript will undergo copyediting, typesetting, and review of the resulting proof before it is published in its final citable form. Please note that during the production process errors may be discovered which could affect the content, and all legal disclaimers that apply to the journal pertain.

performance and cellular structure is a confounding issue for analysis of samples taken from failing human hearts, although this may be overcome with regional analysis by using tagged cMRI and biopsy mapping.

## Keywords

Heart failure; t-tubules; contraction; human

---

## 1. Introduction

The transverse tubules (or t-tubules - TTs) of ventricular myocytes serve to rapidly conduct the cardiac action potential into the cell interior to allow near synchronous  $\text{Ca}^{2+}$  release and contraction [1,2]. TTs can become disorganized and/or lost in animal models of heart failure (for review see [2,3]) and the loss of TTs results in dyssynchronous  $\text{Ca}^{2+}$  release which has been implicated in the contractile deficit of failing myocardium (e.g. [4–6]). Equivalent data for human heart failure is lacking and in view of concerns as to the validity of some animal models for heart failure [7] and the different organization of the TT system in humans compared to smaller animals (e.g. [1,2,8]), data on the extent of possible TT changes in human failure and linkage to contractile performance is highly desirable.

The extent of possible TT loss or reorganization in human heart failure is unclear. Some studies have shown less dense but more dilated TTs [2,3,9–12] while others have reported no change in TT area or volume [4–6,13]. Furthermore, in electron microscopic studies, both TT proliferation [7,14] and loss have been reported [15] while in explanted hearts, no significant TT loss compared to isolated cells was detected [16].

Magnetic resonance imaging studies have shown that contractile performance in the failing myocardium is not uniform [17,18]. We hypothesized that variability in the reported extent of TT remodelling in human (compared to small animal models) might be related to a sampling problem; regions with poor contractile performance might have a different TT structure than regions with stronger contraction and there is heterogeneity in the morphology of TTs in individual patients [10]. Further support for this idea is provided by a rodent study where the extent of contractile deficit was correlated with TT loss [19]. To directly test our hypothesis, we exploited a novel tagged cMRI analysis system coupled with a geometry based tissue sampling method [20] followed by cytochemistry to label TTs and sarcomeres. The resulting images were subjected to detailed image processing to enable a statistical analysis of the relationship between systolic shortening and TT metrics. These novel methods and data identify the best metrics for analysing TT changes and show, for the first time, the relationship between contraction and TT organization in human HF.

## 2. Methods

### 2.1 Ethics, cMRI and biopsy sampling

This study was carried out with the informed, written consent of heart transplant recipients or from the families of organ donors as approved by the New Zealand Health and Disability Ethics Committee (NTY/05/08/050). Normal tissue samples were obtained from unmatched

organ donors. Patients on the cardiac transplantation list with non-ischemic endstage heart failure were imaged with tagged spatial modulation of magnetization (SPAMM) cine magnetic resonance imaging (cMRI) with a 1.5T scanner (Siemens Vision). Regions of interest (ROI) were identified from analysis of circumferential strains in short axis images [21]. Short and long axis untagged cine images were used to create a 3D model of the heart with fiducial markers: Aortic valve, mitral valve, tricuspid valve, pulmonary valve, fibrous base, apex, septum and left ventricle. Superimposed onto the model were the ROI identified in the tagged cMRI sequences. For access to the custom software contact the authors. From the 3D model an azimuthal map was created to guide tissue sampling of the explanted heart as described elsewhere [20]. Subsequently, at transplantation, tissue samples were obtained directly from the operating theatre using the map and immediately fixed in PFA, cryo-protected in sucrose and stored at  $-80^{\circ}\text{C}$ . cMRI was not possible for the normal tissue donors but all donors had a clinically normal echo and EKG. Normal values for tagged MRI and circumferential strain analysis is typically  $\sim 20\%$  [22,23] and all biopsy samples from normal patients are assumed to have generated this strain.

## 2.2 Sectioning and fluorescent labelling

Frozen  $20\ \mu\text{m}$  sections were cut on a Leica CM 1900 cryostat and mounted on polylysine coated coverslips for immunohistochemistry. Cardiac myocytes were labelled for the Z-line ( $\alpha$ -actinin) and t-tubules using wheat germ agglutinin (WGA) using our standard methods [10]. Sections were then incubated with mouse IgG1 anti  $\alpha$ -actinin (1/250, A7811 Sigma-Aldrich) overnight at  $4^{\circ}\text{C}$ . After washing, the sections were incubated with goat anti mouse IgG1 Alexa Fluor 488, and WGA Alexa Fluor 647 (Life Technologies) at room temperature for 2 h (1/200 dilution).

## 2.3 Confocal microscopy and image processing

Fluorescent images of labelled tissue sections were recorded with a Zeiss LSM710 confocal microscope using a Zeiss 60x NA 1.4 oil-immersion objective. Images were acquired with a pixel spacing of 90 nm. Sections which contained cells in a longitudinal orientation were used to obtain at least five randomly selected images covering a field of  $200 \times 200\ \mu\text{m}$ . From each of these images, 10 myocytes were then segmented manually for t-tubule analysis.

Spatial frequency image analysis is used as one metric TT structure [24]. The t-tubule images were converted to frequency space using a fast Fourier transform. The height of the peak in the power spectrum corresponding to the sarcomere spacing (at  $\sim 0.6\ \mu\text{m}$ ) was then estimated by fitting a Gaussian ( $T_{\text{power}}$ ) as illustrated in Figure 1A. An equivalent analysis was performed on images of  $\alpha$ -actinin to generate a measure of Z-line integrity but this was not correlated with  $\%C_c$  and not explored further, although limited dislocations in Z-lines are apparent across the cell. [25]

A second measure of TT abundance is the fractional area occupied by TT staining (illustrated in Figure 1B). This was measured by applying a simple median filter ( $3 \times 3$  pixels) to reduce noise followed by thresholding at the modal intensity plus one standard deviation and

measuring the fraction of pixels above this threshold in the cell image to give  $T_{\text{area}}$ , as illustrated in Figure 1C.

$T_{\text{area}}$  depends on both the apparent width of the TTs and their length. A third estimate of TT abundance was made by taking thresholded image used for  $T_{\text{area}}$  and calculating the fractional area occupied by the topological skeleton ( $T_{\text{skel}}$ ) [24,26]. (see Figure 1D). This measure should more closely reflect the (projected) average length of TTs while  $T_{\text{area}}/T_{\text{skel}}$  should reflect the (possible) dilation of TT widths (note that the diameter of many TTs in human are above the limit of optical resolution [10]).

We previously reported that in human HF, TTs can change direction to become less transverse in orientation [10]. The local angle of TT elements was calculated as follows: At each pixel within the topological skeleton used to calculate  $T_{\text{skel}}$ , a  $5 \times 5$  pixel ROI was extracted, and the angle of this subregion found from the first principal component of the skeleton points in the ROI by singular value decomposition and the angle of the line of best fit was calculated from the coefficients of the principal axis vector. TT segments at  $0^\circ$  angle were parallel to the cells longitudinal axis while those at  $90^\circ$  angle were orthogonal (or transverse) to the cells longitudinal axis (see Figure 1E). The fraction of measured TT angles between 60 and 120 degrees were grouped as being 'transverse' ( $T_{60-120}$ ). This algorithm was implemented in the python programming language using the numpy and scipy packages.

An additional related measure was obtained by applying horizontal and vertical Sobel filters to the topological skeleton (Fig. 1F). The directionality of the skeleton was then expressed as  $T/(T + L)$  where T and L are the number of positive pixels left by the transverse and longitudinal filters, giving a simple measure ( $T_{\text{filt}}$ ) of the relative transverse directionality of the TT network. This method is conceptually simpler and faster than the more precise  $T_{60-120}$  metric or the average direction of TTs calculated from cross correlation with a line mask [10] and  $T_{\text{filt}}$  can be calculated using most image processing packages.

## 2.4 Statistical analyses

Values presented in the text and figures are mean and standard error. Regression as well as classification analysis with the mclust package [27] were carried out in R.

## 3. Results

### 3.1 Tagged cine MRI and local contraction

Figure 2A shows a slice from a typical short axis tagged cMRI sequence of the left ventricle from a diseased heart (with clinical diagnosis of idiopathic dilated cardiomyopathy). From the fitted model dimensions, regions were selected for subsequent sampling (at transplant). Figure 2B shows typical shortening from the regions shown in panel A. The marked difference in contractile performance between regions is apparent with slowed contraction and lower peak shortening in both regions compared to a normal heart (blue trace). Figure 2C shows regional samples of peak contraction from healthy volunteers and heart failure patients. While normal hearts showed typically 20% circumferential contraction ( $C_c$ ), regions of differing contraction were present with the lowest being  $\sim 15\%$   $C_c$ . This is within

the range previously reported for normal hearts [28] but the diseased hearts generally showed much lower strains with some regions barely contracting during systole [17].

### 3.2 Human TT labelling in regions with different contraction

Using our tissue sampling method [20], we took samples from regions with different strains and carried out immunocytochemistry (see Methods). Figure 3A shows exemplar confocal sections of cell surface labelling (WGA) from a normal heart compared to strongly ( $C_c > 12\%$ ) and weakly ( $C_c < 1.8\%$ ) contracting regions from diseased hearts (Figures 3B and 3C respectively). It is visually apparent that there is a loss in TT abundance and organization with disease which appears to parallel the loss of systolic contraction. In contrast to this variable loss of TTs in diseased hearts, the regular sarcomeric actinin labelling was well preserved in the same regions (compare Figures 3D,E,F with Figures 3A,B,C respectively). Therefore, the loss in TT organization and contractile performance was not simply related to a reduction in sarcomeric organization. Additional lower magnification images of TT labelling from patients are shown in Figure 4, which confirms the impression of a general loss and disruption of regular TT labelling with worsening contraction.

### 3.3 TT metrics and regional contraction

The labelled sections were then analysed with the algorithms described in Methods. The results of this analysis are shown in Figure 5 for all patients and samples; the 4 normal hearts are shown in black at 20%  $C_c$  and unique colors for each HF patient (with key to color given in the figure legend). Each metric captured different aspects of the TT derangement;  $T_{\text{power}}$  being related to both longitudinal regularity and abundance,  $T_{\text{area}}$  both TT width and abundance,  $T_{\text{skel}}$  TT length and the new measures  $T_{\text{filt}}$  and  $T_{60-120}$  reporting TT transverse directionality. Figure 5A shows  $T_{\text{power}}$  for all samples and there is a clear positive correlation between shortening and  $T_{\text{power}}$ , although a high degree of variability both within and between patients is evident. Nevertheless for each HF patient (identified by unique colored circles), the visual impression of decreasing t-tubule abundance with worsening contraction is maintained. An alternative measure of the TT extent within the cell is provided by thresholding and measuring the percentage of pixels containing t-tubule label ( $T_{\text{area}}$ ) [13,16]. This measure was also correlated with contraction (Figure 5B) with increased scatter possibly reflecting dilation of remaining t-tubules (see below). The dilation issue is removed by constructing the topological skeleton (Figure 5C), but this did not obviously reduce scatter in the relationship to % $C_c$ .

We have previously reported that in failing samples the TTs may also become misaligned with respect to the z-disk [10,12] and Figure 5D shows the first detailed analysis of the relationship between the fraction of the TT skeleton that was in a transverse direction (i.e. approximately parallel to the z-disk) and local wall shortening. For this measure, the correlation is clearly better than any of the previous measures; the loss of regional contractile performance being closely related to transverse directionality of TTs. While this measure produced precise estimates of t-tubule direction, it was numerically complex so the simpler  $T_{\text{filt}}$  (see Methods) was also applied. Figure 5E shows the relationship between  $T_{\text{filt}}$  and % $C_c$  and while the scatter was increased over  $T_{60-120}$ , this measure also appeared to

be superior to  $T_{\text{power}}$  in its ability to document the degree of TT disarray underlying the change in  $\%C_c$ .

### 3.4 Statistical analysis and classification

We carried out detailed statistical analyses of our data using two separate methods (i) a multivariate linear regression model assuming independent and identically distributed errors and (ii) a conditional inference tree [29] (which is similar to the well-known classification and regression tree (CART) methodology [30]). For the regression, we investigated a number of alternative models, some including log data transformations, but a linear model proved most satisfactory. We started with all TT metrics and then dropped them one by one by using the worst F-statistic to identify a model that had the best fit to regional contractile performance and provide the best definition of ‘t-tubule disease’. Table. 2 summarizes this analysis, showing the final retained metrics, regression coefficients, standard errors and p-values.  $T_{\text{power}}$  and  $T_{60-120}$  were both highly significant predictors for the loss of regional contraction.

The simpler  $T_{\text{filt}}$  measure was also strongly linked to regional contraction (Figure 5E). However, it was also highly co-linear with the more computationally complex  $T_{60-120}$  metric which might be expected since both are measures of TT direction. Thus when both were included in the linear model  $T_{\text{filt}}$  appeared not to be significant when, in fact, it was also a good predictor (i.e.  $T_{\text{filt}}$  without  $T_{60-120}$  was significant at  $p = 7.9 \times 10^{-5}$ ). Since  $T_{\text{filt}}$  is easier to compute, we recommend that it be considered for use in future studies as a quantitative measure of TT disease and is superior to the commonly used  $T_{\text{power}}$  and  $T_{\text{area}}$  metrics. Although the model fitted slightly better when our indirect measure of TT width ( $T_{\text{area/skel}}$ ) was included (and which was kept in the final model), this measure is derived from both  $T_{\text{area}}$  and  $T_{\text{skel}}$  and visual inspection (Figure 4F) suggested that  $T_{\text{area/skel}}$  was not, by itself, tightly linked to  $\%C_c$ .

Analysis of our data with the conditional inference tree method also identified the  $T_{60-120}$  and  $T_{\text{power}}$  variables to be highly influential and the tree fit was slightly better than for linear regression. MRI and modelling studies have shown that a  $\%C_c \sim <10\%$  is associated with an ejection fraction of  $\sim <50\%$ , the latter being a threshold for diagnosis of cardiac myopathy/mild heart failure (e.g. [23,31]) and this  $\%C_c$  is  $>4$  standard deviations below that seen in normal humans [22] and Figure 2C). Using this criterion it is possible to separate the regional samples into near normal (N) and diseased (D) groups. With this definition of disease we could then examine the relationship of our metrics to the disease classification. Since the derangement of TT structure is not easily captured by a single metric, we selected the two best performing metrics that captured TT abundance and directionality ( $T_{\text{power}}$  and  $T_{120-16}$  respectively) and performed a cluster analysis as shown in Figure 6A. From this, a conditional inference tree classification was constructed as shown in Figure 6B, which uses the TT metrics to decide if, from the TT metrics, a  $\%C_c$  of more (N) or less (D) than 10% would have been present (see discussion). Put another way, this the cluster analysis and derived classification tree also defines the extent of ‘t-tubule disease’ (as a structural abnormality) that is associated with significantly impaired contraction (i.e.  $<10\% C_c$  equating to an EF  $<50\%$ ).

## 4. Discussion

We have measured the regional variability in ventricular contraction in human heart failure to examine the link between t-tubule changes and local myocardial performance. This potentially circumvents two major issues in tissue level studies on human heart failure; (i) the difficulty in finding age matched “healthy” tissue and (ii) the confounding effects of the potent drug therapies that heart failure patients receive. We suggest that tissues samples from the failing heart in regions of stronger contraction could be viewed as a differential ‘control’ sample for myocardial disease processes that compromise contractility as they experience the same neuro-humoral and drug environment as regions of much poorer function. This differential analysis then has the potential to distinguish between intrinsic vs. extrinsic factors as well as pathways which are related to impaired contractile performance. Using this approach, we have shown for the first time that contractile function, as measured by tagged cMRI, is strongly associated with TT integrity within failing human hearts.

### 4.1 TT organization and regional Contraction

Although the different TT metrics captured different aspects of TT morphology, in general there is a good correlation between worsening organization/abundance and %C<sub>c</sub>. Unexpectedly, there were areas without obvious TT disruption in regions with good contraction in failing hearts (compare Figure 3A with 3B and Figure 4A,B with 4C, 4G and 4I), which may help explain some previous apparently contradictory results [13,14,16]. In marked contrast to the gross TT disorganization seen in weakly contracting regions, the z-lines and sarcomeric organization appeared generally well preserved in these end-stage failure samples (Figure 3E and 3F).

We found that t-tubule *directionality* ( $T_{60-120}$ ,  $T_{\text{filt}}$ ) was most strongly correlated with local contractile function ( $p < 0.001$ ) in end-stage failure. While measures of TT abundance ( $T_{\text{power}}$ ,  $T_{\text{area}}$  and  $T_{\text{skel}}$ ) also showed significant correlations,  $T_{\text{area}}$  and  $T_{\text{skel}}$  were more weakly linked to contractile performance, a result that may be explained by the problem of thresholding images of a t-system that undergoes dilation (as also suggested by the slope of the relationship between  $T_{\text{area/skel}}$  and %C<sub>c</sub>) and the problem of selecting ‘correct’ thresholds in regions with different labelling intensity -as previously noted [13,16].

### 4.2 Linkage of TT disorganization to regional contraction

Our data strongly support the idea that t-tubule remodeling is responsible for at least a part of the contractile deficit seen in human heart failure [12]. This is likely to arise from both a reduction in the number of dyadic junctions between the t-tubules and sarcoplasmic reticulum (leading to inhomogeneities in Ca<sup>2+</sup> release and the amplitude of the Ca<sup>2+</sup> transient) as well as the different distribution of ion channels that are expressed on the t-tubules compared to sarcolemma [32] which could impact on action potential morphology. Since there was regional variability in the extent of t-tubule disruption in each patient examined, the latter may also contribute to action potential heterogeneity [33] which, along with fibrosis [34], may contribute to the risk for sudden cardiac death.

### 4.3 How might TTs become disorganized?

Since general sarcomeric organization was generally well preserved and did not show a loss in z-line directionality (Figure 3D–F), we conclude that TTs must either become partly detached from their z-line anchors or fail to attach properly to anchors during TT formation. This could be the result of shear forces that will develop between regions of weaker and stronger contraction due to the tissue continuity around the heart. At the cellular level, inhomogeneities in  $\text{Ca}^{2+}$  release due to local loss of TTs [35] may result in differential movement of sarcomeres and this could cause some (unknown) weakening in the protein anchors between z-lines and TT membranes which manifests as a loss in TT directionality and/or abundance. Such an effect would be exacerbated by any misregistration of sarcomeres across the cell [25]. Regardless of the cause, it is well established (from animal models -for review see [5,36]) that such structural abnormalities in TTs will impact on the efficiency of EC coupling and this provides the necessary mechanistic link between the presence of ‘t-tubule disease’ (as defined here from the cellular structural abnormality) and cardiac contractility.

### 4.4 Linking TT disorganization to contractility

As illustrated in Figure 6B, a conditional inference tree can also be used in a diagnostic mode after defining the criterion for disease. Using a reasonable  $C_c$  of  $-10\%$  as a criterion, we showed classification of our regional samples into near normal and diseased groups. It is clear that t-tubule disease is not present in all regions of failing hearts and regions which showed no disease (by this classification) are a major contributor to the contraction of the failing hearts. For a new sample, one can assess the presence of ‘t-tubule disease’ by following the tree from its root, for example, if the  $T_{60-120}$  value is  $>26$  one follows the first left branch, and if  $T_{\text{power}}$  is also  $< 0.69$  the subsequent right branch predicts a likely of  $C_c < 5.8\%$  which would be predictive of a very severe contractile deficit due to TT disruption. This classification tree showed that none of the normal heart donors had evidence for ‘t-tubule disease’ although simply using individual metrics might have suggested otherwise (see distribution of black circles in Fig. 5).

## 5. Conclusion

The methods we have demonstrated here should be applicable to other correlative studies on the cellular and tissue basis of human heart failure. cMRI coupled with regional sampling provides a powerful way to link cellular changes with contractile deficits within single hearts and avoids the uncertainty that random sampling of an inhomogeneous tissue response introduces. It could also be used to examine/rule out the effect of extrinsic factors (such as drugs, neurohumoral status etc.) on cardiac contractility. Finally, it is clear that the progression of ‘t-tubule disease’ in damaged myocardium is inhomogeneous, but likely to be a major factor in the impaired contractility of the failing human heart.

## Acknowledgments

Contract grant sponsor: Health Research Council of New Zealand contract grant number 05-049; National Institutes of Health (NIH); contract grant number: RO1HL087773 and Auckland Medical Research Foundation NZ and Royal Society UK (Wolfson Merit award to MBC).



## Abbreviations

<b>cMRI</b>	tagged cine magnetic resonance imaging
<b>ROI</b>	regions of interest
<b>EKG</b>	electrocardiogram
<b>HF</b>	heart failure
<b>PFA</b>	paraformaldehyde fixative
<b>WGA</b>	wheat germ agglutinin
<b>TT</b>	t-tubule
<b>%Cc</b>	percentage circumferential contraction/shortening

## References

- Cheng H, Cannell MB, Lederer WJ. Propagation of excitation-contraction coupling into ventricular myocytes. *Pflugers Arch*. 1994 Oct; 428(3-4):415-7. [PubMed: 7816564]
- Brette F, Despa S, Bers DM, Orchard CH. Spatiotemporal characteristics of SR Ca<sup>2+</sup> uptake and release in detubulated rat ventricular myocytes. *J Mol Cell Cardiol*. 2005 Nov; 39(5):804-12. [PubMed: 16198369]
- Guo A, Zhang C, Wei S, Chen B, Song L-S. Emerging mechanisms of T-tubule remodelling in heart failure. *Cardiovasc Res*. 2013 May 1; 98(2):204-15. [PubMed: 23393229]
- Louch WE, Mørk HK, Sexton J, Strømme TA, Laake P, Sjaastad I, et al. T-tubule disorganization and reduced synchrony of Ca<sup>2+</sup> release in murine cardiomyocytes following myocardial infarction. *J Physiol (Lond)*. 2006 Jul 15; 574(Pt 2):519-33. [PubMed: 16709642]
- Song LS. Calcium Biology of the Transverse Tubules in Heart. *Annals of the New York Academy of Sciences*. 2005 Jun 1; 1047(1):99-111. [PubMed: 16093488]
- Heinzel, FR.; MacQuaide, N.; Biesmans, L.; Sipido, K. *J Mol Cell Cardiol*. Vol. 50. Elsevier Ltd; 2011 Mar 1. Dyssynchrony of Ca<sup>2+</sup> release from the sarcoplasmic reticulum as subcellular mechanism of cardiac contractile dysfunction; p. 390-400.
- Houser SR, Margulies KB, Murphy AM, Spinale FG, Francis GS, Prabhu SD, et al. Animal models of heart failure: a scientific statement from the American Heart Association. *Circulation research* *Circ Res*. 2012 Jun 22; 111(1):131-50.
- Jayasinghe ID, Crossman DJ, Soeller C, Cannell MB. Comparison of the organization of t-tubules, sarcoplasmic reticulum and ryanodine receptors in rat and human ventricular myocardium. *Clin Exp Pharmacol Physiol*. 2012 Apr 23; 39(5):469-76. [PubMed: 21790719]
- Kostin S, Scholz D, Shimada T, Maeno Y, Mollnau H, Hein S, et al. The internal and external protein scaffold of the T-tubular system in cardiomyocytes. *Cell Tissue Res Springer*. 1998; 294(3): 449-60.
- Crossman, DJ.; Ruygrok, PR.; Soeller, C.; Cannell, MB. Changes in the Organization of Excitation-Contraction Coupling Structures in Failing Human Heart. In: Schwartz, A., editor. *PLoS ONE*. Vol. 6. 2011 Mar 9. p. e17901
- Lyon AR, MacLeod KT, Zhang Y, Garcia E, Kanda GK, Lab MJ, et al. Loss of T-tubules and other changes to surface topography in ventricular myocytes from failing human and rat heart. *Proc Natl Acad Sci*. 2009 Apr 21; 106(16):6854-9. [PubMed: 19342485]
- Cannell MB, Crossman DJ, Soeller C. Effect of changes in action potential spike configuration, junctional sarcoplasmic reticulum micro-architecture and altered t-tubule structure in human heart failure. *J Muscle Res Cell Motil*. 2006 Aug 4; 27(5-7):297-306. [PubMed: 16897575]
- Ohler A, Weisser-Thomas J, Piacentino V, Houser SR, Tomaselli GF, O'Rourke B. Two-Photon Laser Scanning Microscopy of the Transverse-Axial Tubule System in Ventricular Cardiomyocytes from Failing and Non-Failing Human Hearts. *Cardiol Res Pract*. 2009; 2009:1-9.

14. Schaper J, Froede R, Hein S, Buck A, Hashizume H, Speiser B, et al. Impairment of the myocardial ultrastructure and changes of the cytoskeleton in dilated cardiomyopathy. *Circulation*. 1991 Feb; 83(2):504–14. [PubMed: 1991369]
15. Zhang H-B, Li R-C, Xu M, Xu S-M, Lai Y-S, Wu H-D, et al. Ultrastructural uncoupling between T-tubules and sarcoplasmic reticulum in human heart failure. *Cardiovasc Res*. 2013 May 1; 98(2): 269–76. [PubMed: 23405000]
16. Louch W. Reduced synchrony of Ca<sup>2+</sup> release with loss of T-tubules—a comparison to Ca<sup>2+</sup> release in human failing cardiomyocytes. *Cardiovasc Res*. 2004 Apr 1; 62(1):63–73. [PubMed: 15023553]
17. Young AA, Dokos S, Powell KA, Sturm B, McCulloch AD, Starling RC, et al. Regional heterogeneity of function in nonischemic dilated cardiomyopathy. *Cardiovasc Res*. 2001 Feb 1; 49(2):308–18. [PubMed: 11164841]
18. Joseph S, Moazami N, Cupps BP, Howells A, Craddock H, Ewald G, et al. Magnetic Resonance Imaging—based Multiparametric Systolic Strain Analysis and Regional Contractile Heterogeneity in Patients With Dilated Cardiomyopathy. *J Heart Lung Transplant*. 2009 Apr; 28(4):388–94. [PubMed: 19332267]
19. Wei S, Guo A, Chen B, Kutschke W, Xie YP, Zimmerman K, et al. T-Tubule Remodeling During Transition From Hypertrophy to Heart Failure Novelty and Significance. *Circ Res Am Heart Assoc*. 2010; 107(4):520–31.
20. Young AA, Crossman DJ, Ruygrok PN, Cannell MB. Mapping system for coregistration of cardiac MRI and ex vivo tissue sampling. *J Magn Reson Imaging*. 2011 Nov; 34(5):1065–71. [PubMed: 21932357]
21. Young AA. Model tags: direct three-dimensional tracking of heart wall motion from tagged magnetic resonance images. *Med Image Anal*. 1999 Dec; 3(4):361–72. [PubMed: 10709701]
22. Young AA, Li B, Kirton RS, Cowan BR. Generalized spatiotemporal myocardial strain analysis for DENSE and SPAMM imaging. *Magn Reson Med*. 2012 Jun; 67(6):1590–9. [PubMed: 22135133]
23. Maciver DH. The relative impact of circumferential and longitudinal shortening on left ventricular ejection fraction and stroke volume. *Exp Clin Cardiol*. 2012; 17(1):5–11. [PubMed: 23204893]
24. WEI S, Guo A, Chen B, Kutschke W, Xie Y-P, Zimmerman K, et al. T-tubule remodeling during transition from hypertrophy to heart failure. *Circ Res*. 2010 Aug 20; 107(4):520–31. [PubMed: 20576937]
25. Jayasinghe ID, Crossman DJ, Soeller C, Cannell MB. A new twist in cardiac muscle: dislocated and helicoid arrangements of myofibrillar z-disks in mammalian ventricular myocytes. *J Mol Cell Cardiol*. 2010 May; 48(5):964–71. [PubMed: 20045003]
26. Soeller C, Cannell MB. Examination of the transverse tubular system in living cardiac rat myocytes by 2-photon microscopy and digital image-processing techniques. *Circ Res*. 1999 Feb 19; 84(3):266–75. [PubMed: 10024300]
27. Fraley C, Raftery AE. Model-based methods of classification: Using the mclust software in chemometrics. *J Stat Soft*. 2007 Jan; 18(6):1–13.
28. Moore CC, Lugo-Olivieri CH, McVeigh ER, Zerhouni EA. Three-dimensional Systolic Strain Patterns in the Normal Human Left Ventricle: Characterization with Tagged MR Imaging1. *Radiology*. 2000; 214(2):453–66. [PubMed: 10671594]
29. Hothorn T, Hornik K, Zeileis A. Unbiased recursive partitioning: A conditional inference framework. *J Comp Graph Stat*. 2006 Sep; 15(3):651–74.
30. Breiman, L.; Friedman, J.; Stone, CJ.; Olshen, RA. *Classification and Regression Trees*. Chapman and Hall/CRC; 1984. p. 1
31. Hor KN, Wansapura J, Markham LW, Mazur W, Cripe LH, Fleck R, et al. Circumferential strain analysis identifies strata of cardiomyopathy in Duchenne muscular dystrophy: a cardiac magnetic resonance tagging study. *J Amer Coll Cardiol*. 2009 Apr 7; 53(14):1204–10. [PubMed: 19341862]
32. Brette F, Orchard C. T-tubule function in mammalian cardiac myocytes. *Circ Res*. 2003 Jun 13; 92(11):1182–92. [PubMed: 12805236]

33. Lou Q, Fedorov VV, Glukhov AV, Moazami N, Fast VG, Efimov IR. Transmural heterogeneity and remodeling of ventricular excitation-contraction coupling in human heart failure. *Circulation*. 2011 May 3; 123(17):1881–90. [PubMed: 21502574]
34. Wu TJ, Ong JJ, Hwang C, Lee JJ, Fishbein MC, Czer L, et al. Characteristics of wave fronts during ventricular fibrillation in human hearts with dilated cardiomyopathy: role of increased fibrosis in the generation of reentry. *J Amer Coll Cardiol*. 1998 Jul; 32(1):187–96. [PubMed: 9669269]
35. Song LS, Sobie EA, McCulle S, Lederer W, Balke CW, Cheng H. Orphaned ryanodine receptors in the failing heart. *Proc Natl Acad Sci*. 2006; 103(11):4305. [PubMed: 16537526]
36. Orchard CH, Pásek M, Brette F. The role of mammalian cardiac t-tubules in excitation-contraction coupling: experimental and computational approaches. *Exp Physiol*. 2009 May; 94(5):509–19. [PubMed: 19297389]

Author Manuscript

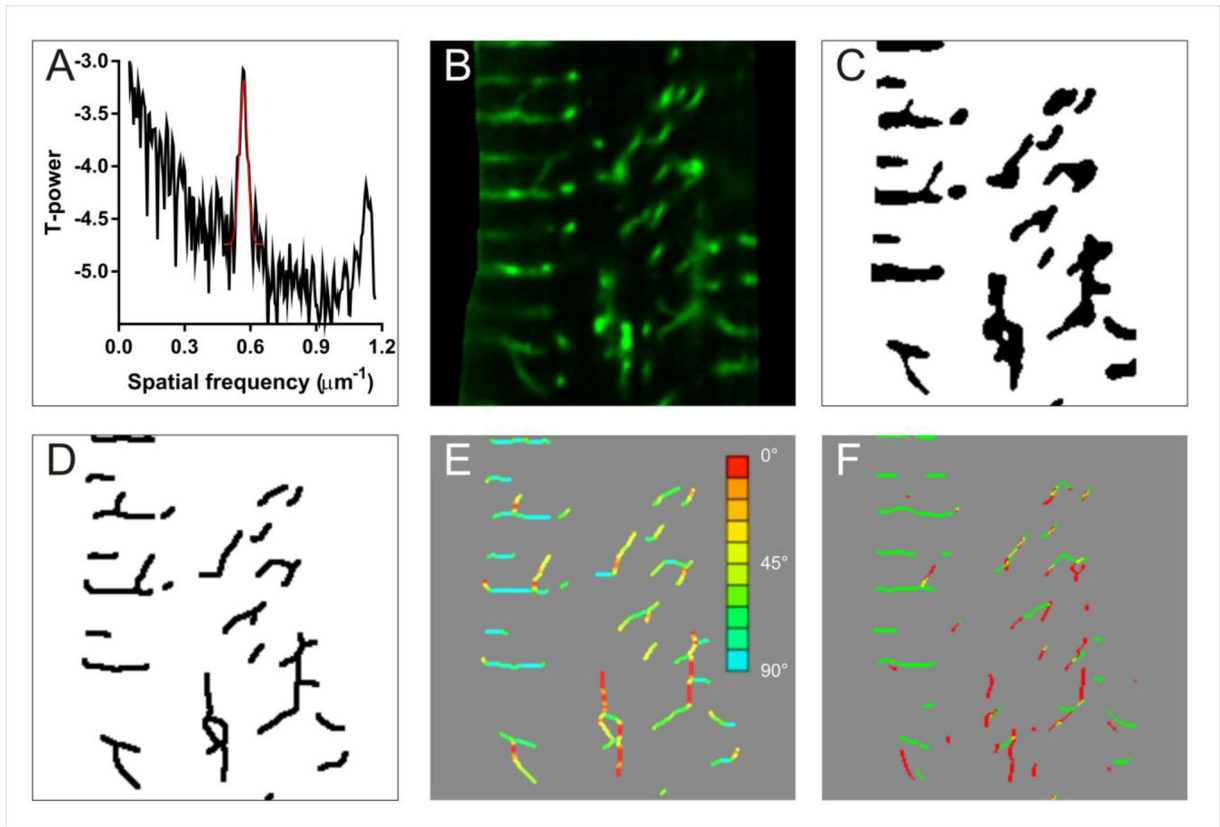
Author Manuscript

Author Manuscript

Author Manuscript

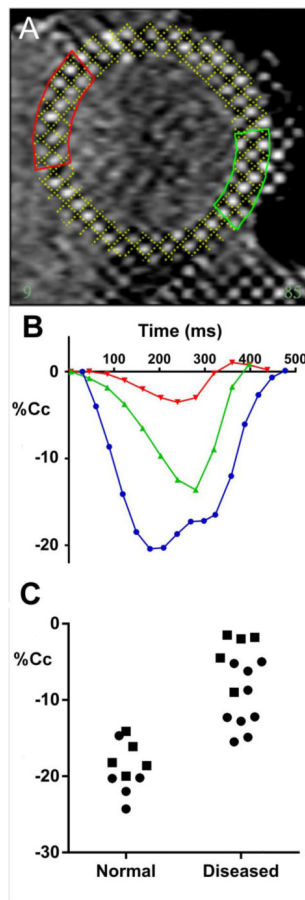
### Highlights

- Tagged cMRI and ventricular tissue biopsy of failing human hearts were performed.
- t-tubules (TT) were labeled and quantified by several structural metrics.
- Regional wall strain and TT structure were generally strongly correlated.
- Statistical cluster analysis allowed construction of a decision tree for disease.
- We conclude that t-tubule disease is likely a major factor in human heart failure



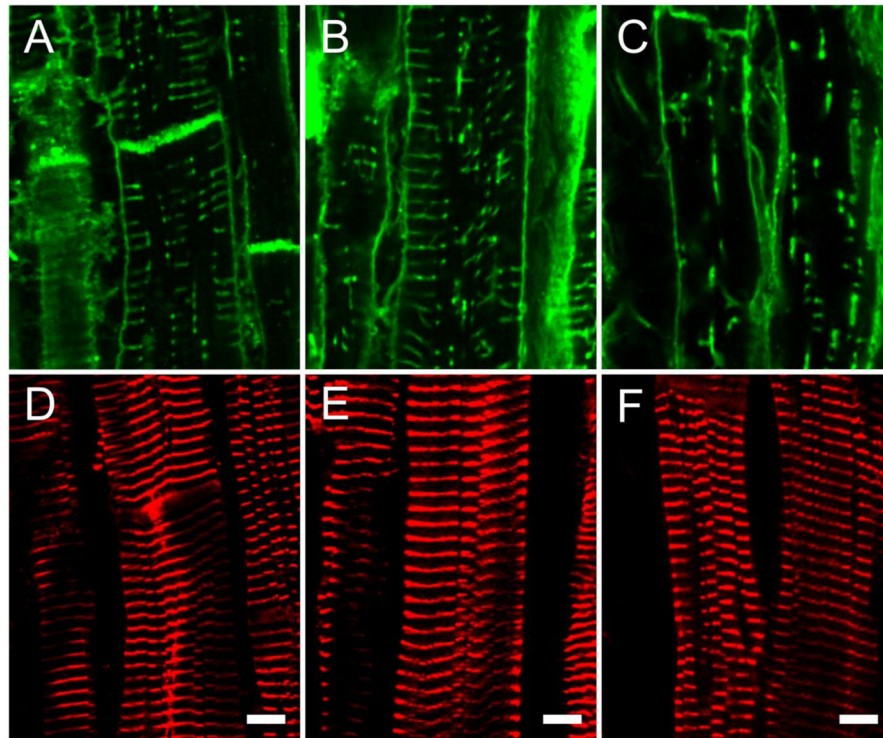
**Figure 1.**

Illustration of image processing methods and derivation of TT metrics. **A** shows a typical power spectrum derived from TT WGA labelling. **B** shows an enlarged region of TT labelling (diseased sample) and **C** the thresholded image. **D** shows the topological skeleton of **C**. The calculated angles of the skeleton are shown in **E** with the color coding shown at right. **F** shows the application of Sobel filters to give transverse (green) and longitudinal (red) skeleton elements.



**Figure 2.**

Regional sampling from cMRI. Panel **A** shows a typical heart short axis view of a patient with idiopathic dilated cardiomyopathy, the tagging marks are fitted by a model computer grid whose dimensions during the contraction/relaxation cycle give regional circumferential contraction (%Cc). **B** shows regional shortening from two regions identified by color in **A**. Note the marked difference in contractile performance between these regions. For reference, shortening from a normal human heart cMRI is shown in blue. Panel **C** shows %Cc a sample of for healthy volunteers and heart failure patients. The symbols denote septum (circles) versus LV free wall (squares).



**Figure 3.** t-tubule and sarcomere labeling. Panels **A,B** and **C** show exemplar confocal micrographs of WGA stained t-tubules from normal, strongly contracting ( $Cc > 12\%$ ) and weakly contracting ( $Cc < 1.8\%$ ) diseased hearts respectively. Panels **D,E** and **F** show z-lines (alpha actinin labelled) of same regions as shown in panels **A, B** and **C** respectively.

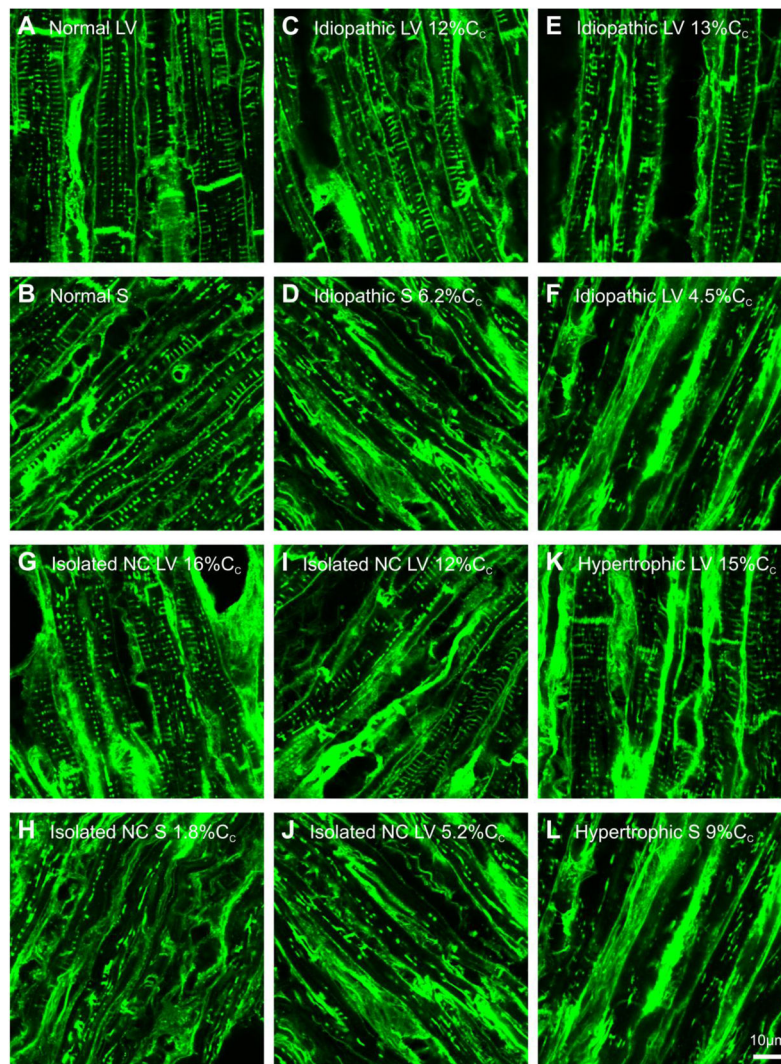


**Figure 4.**

Lower magnification views of WGA labelling of t-tubules in failing human heart regions with variable levels of fractional shortening (% $C_c$ ). Panel **A** shows normal left ventricle (LV) and panel **B** shows normal septum (S) labelling. Panel **C** shows labelling of idiopathic LV (patient 1) with strong fractional shortening (12% $C_c$ ) and panel **D** shows S labelling associated with weak fractional shortening (6.2% $C_c$ ) from the same patient shown in panel **C**. Panel **E** shows labelling of an idiopathic LV (patient 2) with strong fractional shortening (13% $C_c$ ) and panel **F** shows labelling in a region with weak fractional shortening (4.5% $C_c$ ) (same patient shown in panel **E**). Panel **G** shows isolated non-compaction LV (patient 3) with strong fractional shortening (16% $C_c$ ) and panel **H** shows S labelling with weak fractional shortening (1.8% $C_c$ ) (same patient as shown in panel **G**). Panel **I** shows isolated non-compaction LV (patient 4) with strong fractional shortening (12% $C_c$ ) while panel **J** shows LV labelling associated with weak fractional shortening (5.2% $C_c$ ) from same patient shown in panel **I**. Panel **K** shows hypertrophic LV (patient 5) with strong fraction shortening



(15% $C_c$ ) while panel **L** shows S labelling associated with moderate fractional shortening (9% $C_c$ ) from the same patient as shown in panel **K**.

Author Manuscript

Author Manuscript

Author Manuscript

Author Manuscript

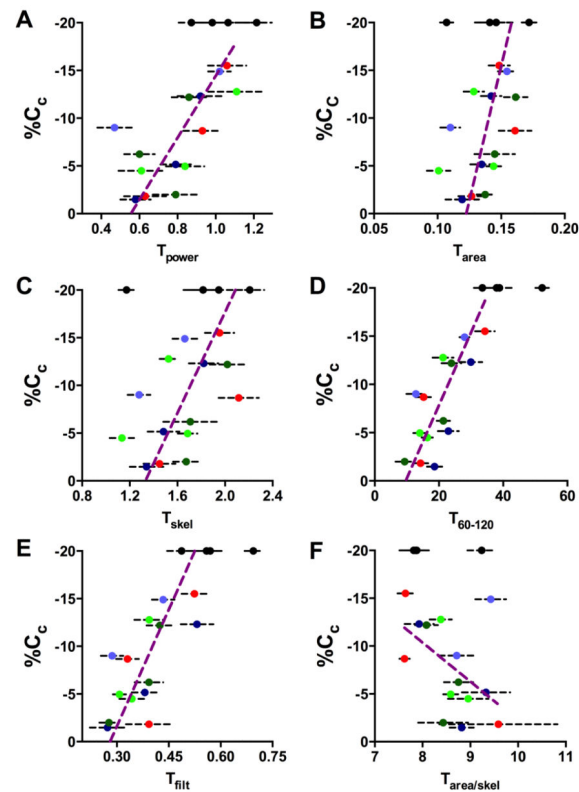


**Figure 5.**

Human t-tubule morphological analysis. Panel **A** shows the relationship between  $T_{\text{power}}$  and %Cc for all samples analyzed. In all panels, each patient is indicated by a different color (see below) and error bars are 1SE. **B**  $T_{\text{area}}$  measured by pixel thresholding. **C**  $T_{\text{skel}}$  measured from the skeleton of the thresholded area image. **D** shows the percentage of TTs that are within 30 degrees of being transverse to the long axis of the cell ( $T_{60-120}$ ). **E** the fraction of energy retained by transverse and longitudinal Sobel filters – note the close similarity of this metric to  $T_{60-120}$  (panel D). **F** shows a proxy for mean TT diameter derived by the division of  $T_{\text{area}}$  by  $T_{\text{skel}}$ . In all panels a Deming regression line is shown to summarise the relationship between the TT metric and %Cc for the diseased samples only with samples from normal hearts being shown by black circles at an assumed 20% Cc. Analysis of samples from patient 1 (table 1) is shown in dark green; patient 2 in light green; patient 3 in red; patient 4 in dark blue; patient 5 in light blue.

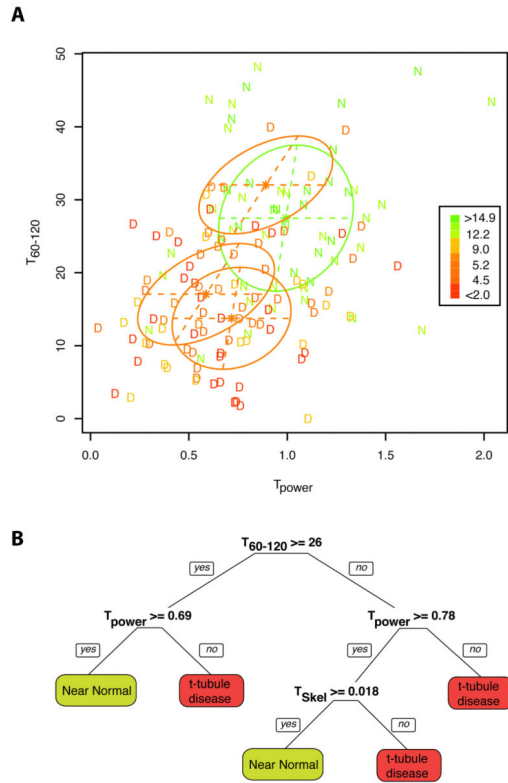


**Figure 6.** Panel A shows all HF samples plotted according to the  $T_{power}$  and  $T_{60-120}$  metrics with D indicating  $Cc < 10\%$  and N indicating  $Cc \geq 10\%$  and coloured according to their  $\%Cc$  values as indicated in the inset. The stars and ellipses show the means and covariances of the best classification with the green ellipse indicating the estimated shape of the N cases and the three red ellipses the same for the D cases. B shows a possible decision tree for t-tubule disease based on the metrics described here.

**Table 1**

Patient details. Abbreviations: LV left ventricle, S septum. Values in parentheses are percent circumferential shortening of the tissue regions analysed

Patient id, Pathology	Age	Sex	Samples analysed	Blood pressure (mmHg)	Medications
1, Idiopathic	21	Male	LV (12), LV (6.2), S (2.0)	90/60	aspirin, bendrofluazide, carvedilol, cilazapril, frusemide, slow-K, spironolactone
2, Idiopathic	49	Female	LV (13), LV (5.0), S (4.5)	96/57	captopril, carvedilol, frusemide, spironolactone, warfarin
3, Isolated non- compaction	35	Male	LV (16), LV (8.7), S (1.8)	90/70	carvedilol, cilazapril, frusemide, warfarin
4, Isolated non- compaction	23	Male	LV (12), LV (5.2), S (1.5)	85/60	aspirin, carvedilol, cilazapril, frusemide, spironolactone
5, Hypertrophic obstructive	52	Male	LV (15), S (9.0)	105/70	carvedilol, frusemide, losartan, simvastatin, spironolactone, warfarin

**Table 2**

Best fit model. TT metrics retained in the final model showing regression coefficients, standard errors and p-values.

Variable	Coefficient	Standard Error	p-value (from F)
Intercept	-6.16	2.23	0.0066
T <sub>power</sub>	-2.70	1.02	0.0087
T <sub>60-120</sub>	-0.18	0.034	$3.1 \times 10^{-7}$
T <sub>area/skel</sub> (TT width proxy)	0.474	0.228	0.039

Author Manuscript

Author Manuscript

Author Manuscript

Author Manuscript